Technical Report

TR-2007-021

Influence of Internal Carotid Artery Geometry on Aneurysm Location and Orientation: A Computational Geometry Study

by

Marina Piccinelli, Susanna Bacigaluppi, Edoardo Boccardi, Bogdan Ene-Iordache, Andrea Remuzzi, Alessandro Veneziani, Luca Antiga

Mathematics and Computer Science

EMORY UNIVERSITY

Influence of internal carotid artery geometry on aneurysm location and orientation: a computational geometry study.

Marina Piccinelli[1,4], Susanna Bacigaluppi[2], Edoardo Boccardi[3], Bogdan Ene-Iordache[1], Andrea Remuzzi[1], Alessandro Veneziani[4,5], Luca Antiga[1]

1. Bioengineering Department, Mario Negri Institute for Pharmacological Research, Bergamo, Italy
2. Università degli Studi di Milano, Clinica Neurochirurgica-Ospedale Policlinico Fondazione IRCCS, Italy
3. Divisione di Neuroradiologia, Ospedale Niguarda Ca' Granda, Milano, Italy
4. MOX (Modeling and Scientific Computing), Dipartimento di Matematica F. Brioschi, Politecnico di Milano, Italy
5. Department of Mathematics and Computer Science, Emory University, Atlanta, GA, USA

Corresponding author:

Dr. Luca Antiga

Medical Imaging Unit, Bioengineering Department

Mario Negri Institute for Pharmacological Research

Centro di Ricerche Cliniche "Aldo e Cele Daccò", Villa Camozzi, 24020 Ranica (BG), Italy

email: antiga@marionegri.it

Abstract

Background and Purpose. The recurrent spatial distribution of cerebral aneurysms sustains the hypothesis of an involvement of hemodynamics in their development. The aim of this paper is to quantitatively characterize the relationships between the three dimensional (3D) geometry of cerebral aneurysms and their parent vasculature in a population of lateral aneurysms located along the internal carotid artery (ICA).

Methods. Patient-specific models of 45 ICA hosting aneurysms were reconstructed from 3D computed rotational angiography images. Using computational geometry techniques, centerlines of all branches and the aneurysm sac were calculated. Position and orientation of aneurysms with respect to the course of the ICA were quantitatively investigated.

Results. The ICA siphon was characterized as a non-planar concatenation of near-planar bends. Aneurysms developed in the distal upper tract of the siphon at sites of local curvature maximum of the hosting bend, along its outer wall. Neck orientation with respect to ICA geometry showed no preferential configuration at the aneurysms site, while a trend to orientate orthogonally to the local osculating plane could be consistently evidenced upstream the ICA course.

Conclusion. 3D geometric relationships between lateral cerebral aneurysms and ICA geometry have been quantitatively assessed, further strengthening the evidence of an existing hemodynamic trigger in aneurysm development and underlining the need for additional investigations on the relationships between geometry and hemodynamics.

Short title:

Keywords:

Word count:

Figures:

Tables:

Introduction

Cerebral aneurysm formation is thought to be the result of an interplay between biomechanical properties of the vessel wall and their possible changes, such as the ones induced by disruption of internal elastic lamina, and local hemodynamic factors, such as wall shear stress and pressure[1,2]. Indeed, the spatial patterns of distribution of aneurysmal lesions in areas subjected to altered hemodynamic forces sustains the hypothesis of a decisive involvement of hemodynamics in the development of cerebral aneurysms. Nowadays, a substantial body of literature, based both on cell culture experiments and computational models[3,4], has lead to the widely accepted notion that hemodynamic forces play a primary role in the initiation, progression and rupture of cerebral aneurysms.

Investigations carried out in the last decade have pointed out that local hemodynamic factors are critically dependent on local vessel geometry and that mild geometric variations in vessel anatomy can significantly alter the resulting flow field and key hemodynamic parameters[5]. In this perspective, the study of the three dimensional (3D) geometry of cerebral aneurysms and their parent vasculature could provide clues to the mechanisms involving hemodynamics in the initiation and development of the pathology.

To date, most of the works dealing with the geometric description of cerebral aneurysms have focused on morphological features of aneurysm sacs, such as size and shape, with the purpose of finding prognostic indexes correlated with risk of rupture or evaluating the efficacy of treatments[6,7,8]. However, in the last years, some authors have recognized the importance of the relation between the complex 3D geometry of the vessels hosting the aneurysms and the location of the aneurysms themselves, and the necessity of quantifying the effects of different geometries on hemodynamic parameters and flow patterns. *Hoi et al*[9] performed computational fluid dynamics (CFD) analyses on idealized models of an aneurysm at different degrees of vessel curvature and aneurysm neck size, postulating a decisive effect of

arterial geometric configurations on the extension of the inflow impact area and ultimately on aneurysm growth processes. *Hassan et al*[10] proposed a classification of the intra-aneurysm hemodynamics based on few simple parent vasculature geometries, rather than on the solely aneurysm morphology, potentially enabling a comparison among different configurations and a stratification for risk of rupture. In a recent paper, *Castro et al*[11] studied the influence of truncation of the parent artery upstream to a lesion on intra-aneurysm hemodynamic parameters, ascribing a determinant role to vessel curvature. In addition, some authors have specifically considered the description of the 3D geometry of cerebral aneurysms and their parent vasculature in order to identify and quantify similar aspects in the spatial patterns of the pathology development. *Ingebrigsten et al*[12] used 3D digital subtraction images of cerebral circulation to measure vessel radii and bifurcation angles, hypothesizing that the presence of cerebral aneurysms is associated with deviations from the optimal (i.e. work-minimizing) bifurcation geometry. In *Sadatomo et al*[13] and *Sakamoto et al*[14], terminal aneurysms located at middle cerebral artery and internal carotid artery bifurcations were considered: instead of developing in front of the apex, aneurysm necks seemed to deviate to the side of one daughter artery. *Kasuya et al*[15] studied the anterior communicating artery complex, measuring the angle between the A1 and A2 segments and discussing the relationship between the angle between the arteries and the corresponding incidence of aneurysms.

One of the main obstacles associated with the characterization of cerebro-vascular geometry is the great anatomical inter-individual variability. As a consequence, in order to enable quantitative comparisons of geometric features across a wide population, standardized and robust methods for geometric quantities definition and measurement are in order[16,17].

In this paper, we characterized the geometry of aneurysms and their parent vasculature in a population of lateral aneurysms located along the internal carotid artery (ICA) siphon. There's a common anecdotal evidence that ICA lateral aneurysms preferentially arise on the outer

wall of carotid siphon bends, as a result of sustained hemodynamic stresses occurring at these locations. The aim of this study was to quantify position and orientation of this type of aneurysms with respect to the course of the ICA, in order to characterize the spatial patterns of aneurysm development and consequently contribute to the search for hemodynamic triggers. Patients were selected from a population of consecutive subjects that underwent three-dimensional computed rotational angiography (3D CRA) for the assessment of cerebral aneurysms following clinical routine. Image-based geometric characterization was performed using a previously introduced computational framework[16].

This work has originated within the ANEURISK study[18], a wider project on development of geometric, biomechanical, computational and statistical tools for the analysis of cerebral aneurysms and their parent vasculature.

Materials and Methods

Patient population and image acquisition

Between September 2002 and September 2006, 134 patients underwent 3D CRA for assessment of cerebral aneurysms at the Neuroradiology Division of the Niguarda Ca' Granda Hospital in Milan following clinical routine. Among these, 45 patients with lateral aneurysms along the ICA were considered eligible for inclusion in the study, while 4 patients were excluded because of absence of anterior cerebral artery (ACA) perfusion. Patient demographic data, occurrence of aneurysms and aneurysm rupture are summarized in Table 1.

Rotational angiography images were obtained with an Integris Allura Philips Unit (Netherlands) with the following parameters: C-arm rotation speed 55 deg/s, matrix size 512x512 pixels, frame rate 25 frames/s. Prior to acquisition, 18 ml of nonionic hydrosoluble contrast agent were injected at 4 ml/s with a catheter positioned in the ICA or in the vertebral artery, providing continuous filling of cerebral vessels. All images were reviewed by an expert radiologist (EB) that provided information whether the aneurysms were ruptured or unruptured. After reconstruction, 3D CRA images were collected in DICOM format for 3D vascular modeling and geometric characterization.

3D modeling

Patient-specific models of ICA hosting aneurysms were reconstructed from 3D CRA images. Segmentation was performed using implicit deformable models[21,22]. A surface representing the vessel boundary was defined at the location of the steepest change in intensity at the periphery of the lumen. The segmentation tool employed is part of an open source project for vascular modeling[20] and it relies on the Insight Toolkit library[19].

The aneurysm sac and the ICA including its bifurcation into ACA and middle cerebral artery (MCA) were reconstructed for every subject. The length of the proximal portion of ICA

included in the 3D models depended on the extent and location of the field of view (FOV) employed during acquisition, which in turn depended on aneurysm location; a minimum of 26 mm was included in all models.

Geometry characterization

In a previous work, *Antiga et al*[16] proposed a computational framework for geometric characterization of bifurcating vascular segments. In the following, we briefly recall the main concepts and refer to the cited paper for technical details.

Centerline computation. A centerline is a line traced between two endpoints that maximizes the minimal distance from the boundary of a tubular structure, and it is computed solving a minimal cost problem on the medial surface of the vessel shape[16]. Every point of such computed centerline hosts the center of a sphere maximally inscribed in the vessel. Each maximally inscribed sphere provides a quantification of vessel size, since its radius corresponds to the minimum projection diameter employed in evaluation of multiple-projection X-ray angiography. Centerlines were calculated for all branches (ICA, MCA, ACA) and for the aneurysm sac; for this latter case, the endpoint on the aneurysm surface was selected as the farthest point from the neck section, so that the resulting centerline ran throughout the sac. The reason for considering the aneurysm sac as a vascular segment with its own centerline fulfills the need for a description of the aneurysm neck region and its orientation with respect to the parent vessel, as described in the following sections. From now on, we will refer to the bifurcation between the ICA centerline and the aneurysm centerline as the *aneurysm* bifurcation (Figure 1A).

ICA geometry. Length, curvature and torsion were computed for the centerline relative to each ICA. A curvilinear abscissa s was defined along the ICA centerline and the s=0 location was set at the ICA bifurcation. This location furnishes a good reference point even for a population featuring strong anatomical variability. *Curvature* and *torsion* were then computed

using classical expressions[23]. Curvature equals the reciprocal of the radius of the tangent circle that lies in the plane that locally hosts the curve, the so-called *osculating plane*; torsion is the quantity characterizing the rate of rotation of the osculating plane, taken positive for counter-clockwise rotations. Prior to the computation of curvature and torsion, all centerlines were smoothed with a Laplacian filter, in order to account only for their major geometric features.

ICA Frenet frame. To describe the local 3D geometry of the carotid siphon, the Frenet frame was built along each ICA centerline. The Frenet frame is identified by the tangent unit vector $\mathbf{t}_{ff}$ and by two unit vectors, the binormal $\mathbf{b}_{ff}$ and the normal $\mathbf{n}_{ff}$, lying on the plane normal to $\mathbf{t}_{ff}$. At every point, $\mathbf{n}_{ff}$ is directed toward the center of the osculating circle of the curve, while $\mathbf{b}_{ff}$ is locally aligned with the normal to the osculating plane (Figure 1B).

In order to identify the major bends of the siphon along the ICA, we subdivided the ICA centerline on the basis of curvature and torsion. Locations of local curvature maxima and both torsion maxima and minima were determined. Each bend was defined around a point of maximum curvature and delimited by the two (proximal and distal) closest torsion peaks. To allow comparisons amongst patients, corresponding bends were identified on all centerlines.

Bifurcation reference system and branch vectors. Based on calculated centerlines, local reference systems were defined at both the ICA and the aneurysm bifurcations of each model. Bifurcation reference systems were computed according to the criteria introduced by *Antiga et al*[16], and are composed by an origin **o** and two unit vectors, the bifurcation normal $\mathbf{n}_b$ and up-normal $\mathbf{u}_b$, the first identifying the plane in which centerlines lie while departing from each other and the second lying on the bifurcation plane and pointing downstream. The direction of each branch coming off the bifurcation was characterized by means of a vector, the *branch vector*, defined from the first point of the branch centerline up to a point one inscribed sphere radius away from the bifurcation.

By means of the bifurcation reference system relative to the aneurysm bifurcation, the position and orientation of the aneurysm neck with respect to the ICA could be quantified. The origin of

the reference system accounts for the position of the aneurysm neck along the siphon centerline ($\mathbf{o}_{an}$), the normal to the bifurcation plane represented the aneurysm neck orientation ($\mathbf{n}_{an}$) and the branch vector relative to the aneurysm centerline identified the main direction of the sac just distal to the neck ($\mathbf{v}_{an}$) (see online additional materials: Figure AM1). Even if aneurysm sacs cannot in general be described as tubular structures, the definition of the first tract of the centerline within the sac, which crosses the neck and identifies the bifurcation plane orientation, was robust to the selection of the corresponding endpoint[1] (see online additional materials: Figure AM1). For this reason, the aneurysm branch vector accounted for the direction of the proximal portion of the aneurysm sac even in presence of complex lesion shapes.

To characterize the location of the aneurysms along the ICA, two geometric parameters were investigated: (i) the curvilinear abscissa of the neck $\mathbf{o}_{an}$ along the ICA; (ii) the relative distance, in terms of curvilinear abscissa, between the aneurysm neck $\mathbf{o}_{an}$ and the curvature maximum identifying the bend. The former provides an overall indication of the aneurysm position along the ICA, while the latter furnishes an insight on the position of the lesion within the single bend.

In each model, the orientation of the aneurysm sac at the aneurysm origin was investigated by comparing the aneurysm branch vector $\mathbf{v}_{an}$ and the Frenet curve normal $\mathbf{n}_{ff}$ at $\mathbf{o}_{an}$; the two vectors were projected onto the bifurcation plane and their dot product computed. Depending on the sign of the result, the aneurysm was classified as directed towards the inner (-) or the outer (+) wall of the parent vessel. To characterize the orientation of the neck with respect to the local osculating plane, the angle between the Frenet curve binormal $\mathbf{b}_{ff}$ at $\mathbf{o}_{an}$ and the aneurysm bifurcation normal $\mathbf{n}_{an}$ was calculated (Figure 1C). The computed angle was converted to the 0-90° range to synthetically represent the deviation of the bifurcation plane

1 This is an effect of the adopted definition of centerline, which is generated on top of the Voronoi diagram associated with the model shape. This ensures that the centerline is medial with respect to the neck independently of the endpoint chosen[16].

from the local osculating plane.

To characterize the influence of the upstream ICA geometry on aneurysm orientation, the aneurysm bifurcation normal $\mathbf{n}_{an}$ and the osculating plane normal $\mathbf{b}_{ff}$ computed at locations 2mm, 4mm, 6mm and 8mm upstream the aneurysm neck $\mathbf{o}_{an}$ were compared. To correctly calculate the angle between each pair of vectors, which were defined at different locations along the ICA centerline, the *parallel transport* technique was employed, as previously described[17]. With this approach, $\mathbf{n}_{an}$ was transported along the centerline to the point of application of $\mathbf{b}_{ff}$ without introducing torsion; the angle between $\mathbf{b}_{ff}$ and the transported normal $\mathbf{n}_{an\text{-}pt}$ was then computed (Figure 1D) and subsequently converted to the 0-90^{o} range.

Data Analysis

Statistical analysis was performed using the R statistical package[24]; *t*-test, Fisher's exact test, *chi-square* test and Pearson's correlation were used where appropriate, as indicated in the Results. Throughout the paper, descriptive statistics will be presented as *mean(standard deviation)*.

Results

3D model reconstruction and centerline computation.

All models of ICA with lateral aneurysms included in the study were reconstructed from DICOM images for a total of 45 models (see Table 1 and online additional materials Figure AM2). Depending on the acquisition FOV, the length of the reconstructed carotid siphons varied from a maximum of 113 mm to a minimum of 26 mm proximal to the ICA bifurcation (mean 69.5 (21.8) mm); the mean radius of siphons was 1.87 (0.21) mm, in accordance with the value of about 2 mm commonly found in the literature[25].

Siphon bend identification.

The number of peaks extracted from the curvature profiles, and consequently the number of bends, changed from case to case even in models of comparable lengths, due to anatomical differences in ICA course. To quantify such variability we took into consideration the patients with a scanned ICA length of at least 60 mm (n=34, 74% of the total number of subjects) and sextracted the curvature peaks of the siphon centerline from the ICA bifurcation back to the point of abscissa 60 mm; out of the selected 34 models, 18 centerlines exhibited 5 peaks, 7 centerlines 4 peaks, 6 centerlines 6 peaks, and the remaining two cases 3 and 7 peaks respectively. Analysis of torsion underlined the presence of frequent fluctuations from positive to negative values along the siphon centerlines, which indicated frequent revolutions of the osculating planes of successive bends around the centerline. In general, two different kinds of torsion extrema were identified: (i) small absolute value peaks, due to minor anatomical features; (ii) high absolute value peaks, which indicated the locations of major changes of osculating plane orientations. Taking into account the profiles of both curvature and torsion revealed that the points of maximum curvature corresponded to low torsion values, usually near zero, while torsion peaks matched points of curvature minima, as shown in Figure 2A for an explanatory case. To quantify this finding, torsion values of all curvature

peaks and curvature values for all torsion peaks were considered and their ratios to the absolute torsion peak and the absolute curvature peak, respectively, were computed. The results are shown in Figure 2B. It follows that the carotid siphon can be described as a sequence of near-planar bends separated by sudden changes in the osculating plane orientation (Figure 3).

A high heterogeneity in the extent and shape of bends was found, in accordance with the observation on the distribution of curvature peaks made above. In Figure 4, the length of bends identified on each centerline are plotted from the most proximal (bend 6) to the most distal (bend 0, adjacent to the ICA bifurcation). Despite the high variability, the analysis of curvature profiles of all centerlines revealed similar patterns, with a high curvature peak always recognizable, corresponding to a sudden *c-shaped* bend in the models, often preceded by another peak of similar value. Anatomically, this curve corresponded to the final bend of the cavernous segment of the ICA, where anatomical constraints, the posterior and anterior clinoid processes of the sphenoid bone, force the artery to take two sharp curves, with a course similar to an italic *s*, before entering the intra-cerebral space; in the following we will refer to this bend as the *C* bend. All models included the cavernous segment; in two cases the curvature peak of the *C* bend couldn't be identified because of the presence of a giant aneurysm that compromised the original anatomy of the artery to a very high degree. Although the abscissa and curvature value of these higher peaks varied among patients, they were on average located around a mean value of 23.6 (4.03) mm from the ICA bifurcation. Along the tract from the *C* bend to the ICA bifurcation, one or two bends were usually identified depending on the patient ICA anatomy; in one case three bends were identified. Due to the constant presence of the *C* bend and to its anatomical significance, this bend was taken as a reference; the bends proximal and distal to the *C* bend were then numbered accordingly (e.g. first proximal bend or second distal bend).

Aneurysm position along the ICA centerline. In Figure 5, the curvilinear abscissa of $\mathbf{o}_{an}$, the origin of the aneurysm neck, is plotted for all aneurysms. Lesions showed to develop in the distal upper tract of the carotid siphon, at a mean abscissa of 12.5 (8.6) mm from the bifurcation point. In the figure, the distinction between ruptured and unruptured aneurysms is also displayed. It is worth pointing out that in the cases collected in the present study, ruptured aneurysms appear to be located at higher abscissas with respect to unruptured aneurysms. The *t*-test comparing the mean abscissa values revealed significant differences between the two groups ($p<0.05$).

In the 44 models on which the *C* bend was identified, the distribution of aneurysms on bends was investigated considering the proposed subdivision of siphon in *C* bend, proximal and distal bends; the results are shown in Figure 6. The majority of aneurysms developed on the *C* and distal bends, while only two lesions grew proximal to the *C* bend. Except for one case, all ruptured aneurysms developed in the distal bends and predominantly (8 aneurysms out of 15) on the first bend distal to the *C* bend. In order to test for the difference in the distribution of ruptured and unruptured aneurysms on the siphon bends, Fisher's exact test showed significant differences between the distributions of the two groups ($p < 0.05$). Of note, no ruptured aneurysms were located on the *C* bend.

Last, the location of aneurysms inside the hosting bends was evaluated. The majority of lesions developed at the site of local curvature maximum within the bend or within one diameter (~4 mm) from it, as shown in Figure 7. The mean distance of ruptured aneurysms from the local curvature maximum was not significantly different from zero (*t*-test, $p=0.6$), while there was statistical significance for the unruptured aneurysm group (*t*-test, $p=0.01$).

Aneurysms orientation with respect to the ICA. The computation of the orientation of the aneurysm neck with respect to the parent vessel indicated that lesions grew predominantly along the outer wall of the ICA. Out of 46 aneurysms, only 4 lesions were oriented towards

the inner wall of the ICA.

The orientation of aneurysm necks with respect to the upstream ICA geometry is displayed in the sequence of histograms in Figure 8, where the angle between $\mathbf{b}_{ff}$ and $\mathbf{n}_{an\text{-}pt}$ is computed between 0 and 8 mm proximal to the neck at regular intervals of 2 mm, taken as an approximation of the mean siphon radius.

No preferential configuration could be evidenced as to the orientation of aneurysm necks at the site of lesion: as displayed in Figure 8, the computed angles between $\mathbf{b}_{ff}$ and $\mathbf{n}_{an}$ cover almost the whole 0-90º range, with a minor tendency not to orientate orthogonally to the local osculating plane.

The angle distributions show a gradual trend of the aneurysm bifurcation plane to be orientated orthogonally to the local osculating plane. This trend reaches its maximum at 4 mm upstream the neck, i.e. one diameter from it. Further upstream, angles progressively lose coherence and roughly cover the entire 0-90º range at 8 mm. Angle distributions were tested for uniformity with a chi-squared test. All distributions were not significantly different from uniform except for the one computed at 4mm upstream the aneurysm site, for which there was highly statistical significance ($p<0.001$).

To gain further insight on the results obtained at this location, we considered the change in the osculating plane orientation between the 0 and 4 mm locations ($\Delta\alpha_{op}$), i.e. the difference between the angle calculated between $\mathbf{b}_{ff}$ and $\mathbf{n}_{an}$ at the lesion site, $\alpha(\mathbf{b}_{ff},\mathbf{n}_{an})_{lesion\ site}$, and the angle computed between $\mathbf{b}_{ff}$ and $\mathbf{n}_{an\text{-}pt}$ at 4 mm upstream the lesion site, $\alpha(\mathbf{b}_{ff},\mathbf{n}_{an\text{-}pt})_{at\ -4mm}$. Statistical analysis showed a significant correlation between $\Delta\alpha_{op}$ and the deviation of the aneurysm bifurcation plane from the local osculating plane at the lesion site (see Figure 9). For values of $\Delta\alpha_{op}$ greater than 45º (i.e. for considerable changes in the osculating plane orientation) deviations of the aneurysm bifurcation plane from the local osculating plane were small, while greater deviations were associated to values of $\Delta\alpha_{op}$ smaller than 45º (Pearson's correlation

coefficient r=-0.72, $p<0.001$).

Discussion

Recurrent patterns in the distribution of cerebral aneurysms and the established relationships between geometry and hemodynamics and between hemodynamics and blood vessel wall function have contributed evidence for a hemodynamic trigger among the processes involved in aneurysm formation. In this context, the characterization of the geometry of cerebral aneurysms and their parent vasculature is of central importance, as the identification of geometric patterns may point to hemodynamics-related mechanisms in the development of cerebral aneurysms.

In recent studies several authors have emphasized the effects of geometric features of cerebral aneurysms and their parent vasculature on the hemodynamic flow field[9,10,11], while others have explicitly focused on the extraction of parameters characterizing aneurysm shape and dimensions[6,7,8] and the geometry of their parent vasculature[12,13,14,15].

In the present paper, some of the complex geometric relationships between cerebral aneurysms and their parent vessels are quantitatively documented on a population of ICA lateral aneurysms through the application of rigorous geometric criteria[16]. For each patient investigated in our study, a 3D model of the ICA hosting the aneurysm was reconstructed, centerlines of the carotid siphon and the aneurysm sac were calculated and the aneurysm bifurcation defined. Curvature and torsion of each siphon centerline were computed and employed to identify individual siphon bends. The position of the aneurysm neck along the carotid siphon and its orientation with respect to the ICA were finally evaluated.

The analysis of curvature and torsion of ICA centerlines allowed to describe the carotid siphon as a sequence of near-planar bends separated by sudden changes in the orientation of their osculating plane (Figure 3). This finding highlights the relevance of non-planarity in the geometry of the carotid siphon and provides a guide for future studies aimed at elucidating the influence of non-planarity on local hemodynamics[26]. Indeed, in a recent paper, *Lee et al*[27] studied the effects of double bends on hemodynamics paying particular attention to non-planar configurations. In their computations the second bend influences the final flow patterns to a

different extent depending on the orientation of its osculating plane with respect to the first bend, unveiling some of the complex phenomena influencing hemodynamics in the carotid siphon.

The position of the aneurysm neck along the siphon centerline was extracted for all models in terms of curvilinear abscissa and distribution on the siphon bends. In our sample, lesions preferentially arose in the distal portions of the ICA (Figure 5). Even though the clinical indication for 3D CRA may have had an effect on this datum, worth noting is the preferential location of lesions in the intra-cerebral space, especially for the ruptured aneurysms group, where hemodynamic forces may have a stronger effect due to the structural properties of the surrounding tissues. The position of aneurysms inside their hosting bends revealed, in accordance to anedoctal evidence, that aneurysms preferentially localize close to the point of local curvature maximum (Figure 7), where the region of flow impingement is expected to be located.

The orientation of aneurysms was then evaluated in terms of direction of the main axis of the aneurysm sac with respect to the parent vessel wall and in terms of deviation of the aneurysm bifurcation plane from the local ICA osculating plane. As expected, almost all aneurysm necks were located on the outer wall of the ICA bends, where the action of hemodynamic forces is stronger due to the high vessel curvature. On the contrary, we found no evidence of a tendency of the aneurysm neck to lie on the local osculating plane, as one would expect by considering the hemodynamic stresses on the outer wall of a curved vessel. We instead found that the angle between the aneurysm neck and the local osculating plane are almost uniformly distributed over the range 0-90^{o} (Figure 8). The study of the upstream ICA geometry, however, revealed a statistically significant trend of aneurysms to orientate orthogonally to the osculating plane one diameter upstream the neck, a trend that disappears further upstream (Figure 8). These results suggest the need for further characterizations of the complex hemodynamics arising from non-planar concatenations of bends.

A deeper analysis of these results indicated that, for abrupt variations in the orientation of the ICA osculating planes within one diameter upstream the lesion site, the aneurysm neck orientates predominantly on the local osculating plane, while for less significant variations the deviation of aneurysm bifurcation plane from the osculating plane covers a wider range of values (Figure 9). The previously cited paper of *Lee at al*[27] on the effects of non-planar configurations of double bends on hemodynamics patterns can give some insight into the explanation of our findings. In that work, the introduction of non-planarity between the first and the second bend was found to break the symmetry between the two Dean vortices established at the first bend, strengthening the outer vortex on the second bend with respect to the inner one and resulting in increased mechanical forces on the outer wall of the second bend. This is in principle consistent with our results, that show that the aneurysm neck preferentially lies in the local osculating plane in case of abrupt changes in the orientation of upstream osculating planes. On the contrary, a near-planar arrangement of two successive bends leads to less defined vortex structures, with the generation of secondary and tertiary vortices at the second bend, and consequently to a greater variability in the localization of hemodynamics forces at the wall. This is also in accordance with our results, that show uniformly distributed orientation of aneurysm necks around the wall in presence of small variations in the ICA upstream geometry.

The results presented in this paper provide further evidence of an existing hemodynamic trigger for aneurysm formation and underscore the need for additional investigations in order to clarify and quantify the complex relations between geometry and hemodynamics. Although of interest, this cross-sectional study may be affected by few limitations related to the sample size and composition. Patients were selected from a wide population that underwent 3D CRA following clinical routine, but indication for 3D CRA sometimes implies the presence of large aneurysms whose dimensions may have altered the original anatomy of the parent vasculature. The presence of a few large necks, hardly distinguishable from the parent vessel, may in a few cases

have had an effect on the computation of the orientation of the aneurysm bifurcation. The availability of high-resolution CT and MR scanners will make it possible to extend the investigation to a larger number of subjects and decrease the bias in the selection of the population. This will be subject of future work.

Conclusions

In this paper, we characterized geometric relations between cerebral aneurysms located on the ICA and their parent vessel, showing the existence of recurrent geometric patterns and suggesting how they may be suggestive of hemodynamics triggers that contribute to aneurysm development. These preliminary results emphasize the need for future extensive studies on the relationships linking vessel anatomy to hemodynamic flow patterns and, ultimately, to aneurysm development mechanisms.

Acknowledgments

The ANEURISK project is supported by a grant from the Politecnico di Milano Foundation and Siemens Italia Medical Solutions.

References

1. Suarez JI, Tarr RW, Selman WR. Aneurysmal subarachnoid hemorrhage. *N Engl J Med* 2006; 354:387-96.
2. Van Gijn J, Kerr RS, Rinkel GJ. Subarachnoid haemorrhage. *Lancet* 2007; 369:306-18.
3. Cebral JR, Castro MA, Appanaboyina S et al. Efficient pipeline for image-based patient-specific analysis of cerebral aneurysm hemodynamics: technique and sensitivity. *IEEE Trans Med Imaging* 2005; 24(4):457-67.
4. Steinman DA, Milner JS, Norley CJ et al. Image-based computational simulation of flow dynamics in a giant intracranial aneurysm. *AJNR Am J Neuroradiol* 2003; 24(4):559-66.
5. Friedman MH. Variability of 3D arterial geometry and dynamics, and its pathologic implications. *Biorheology* 2002; 513-517.
6. Raghavan ML, Ma B, Harbaugh RE. Quantified aneurysm shape and rupture risk. *J Neurosurg* 2005; 102(2):355-62.
7. Ma B, Harbaugh RE, Raghavan ML. Three-dimensional geometrical characterization of cerebral aneurysms. *Ann Biomed Eng* 2004; 32(2):264-73.
8. Parlea L, Fahrig R, Holdsworth DW et al. An analysis of the geometry of saccular intracranial aneurysms. *AJNR Am J Neuroradiol* 1999; 20(6):1079-89.
9. Hoi Y, Meng H, Woodward SH et al. Effects of arterial geometry on aneurysm growth: three-dimensional computational fluid dynamics study. *J Neurosurg* 2004; 101(4):676-81.
10. Hassan T, Timofeev EV, Saito T et al. A proposed parent vessel geometry-based categorization of saccular intracranial aneurysms: computational flow dynamics analysis of the risk factors for lesion rupture. *J Neurosurg* 2005; 103(4):662-80.
11. Castro MA, Putman CM, Cebral JR. Computational fluid dynamics modeling of intracranial aneurysms: effects of parent artery segmentation on intra-aneurysmal hemodynamics. *AJNR Am J Neuroradiol* 2006; 27(8):1703-9.
12. Ingebrigtsen T, Morgan MK, Faulder K et al. Bifurcation geometry and the presence of

cerebral artery aneurysms. *J Neurosurg* 2004; 101(1):108-13.

13. Sadatomo T, Yuki K, Migita K et al. Evaluation of relation among aneurysmal neck, parent artery, and daughter arteries in middle cerebral artery aneurysms, by three-dimensional digital subtraction angiography. *Neurosurg Rev* 2005; 28(3):196-200.
14. Sakamoto S, Ohba S, Shibukawa M et al. Characteristics of aneurysms of the internal carotid artery bifurcation. *Acta Neurochir* 2006; 148(2):139-43.
15. Kasuya H, Shimizu T, Nakaya K et al. Angeles between A1 and A2 segments of the anterior cerebral artery visualized by three-dimensional computed tomographic angiography and association of anterior communicating artery aneurysms. *Neurosurgery* 1999; 45(1):89-93.
16. Antiga L, Steinman DA. Robust and objective decomposition and mapping of bifurcating vessels. *IEEE Trans Med Imaging* 2004; 23(6):704-13.
17. Thomas JB, Antiga L, Che SL et al. Variation in the carotid bifurcation geometry of young versus older adults: implications for geometric risk of atherosclerosis. *Stroke* 2005; 36(11):2450-6.
18. ANEURISK Project Website. Available at: http://www2.mate.polimi.it:8080/aneurisk. Accessed October 12, 2007.
19. The Insight Segmentation and Registration Toolkit. Available at: http://www.itk.org. Accessed October 12, 2007.
20. Vascular Modeling Toolkit. Available at: http://vmtk.sourceforge.net. Accessed October 12, 2007.
21. Sethian JA. A fast marching level set method for monotonically advancing fronts. *Proc Natl Acad Sci USA* 1996; 93(4):1591-5.
22. Antiga L, Ene-Iordache B, Remuzzi A. Computational geometry for patient-specific reconstruction and meshing of blood vessels from MR and CT angiography. *IEEE Trans Med Imaging* 2003; 22(5):674-84.
23. Wolfram MathWorld. Available at: http://mathworld.wolfram.com. Accessed October 12,

2007.

24. R Development Core Team (2007). R: A language and environment for statistical computing. R Foundation for Statistical Computing, Vienna, Austria. Available at: http://www.R-project.org. Accessed October 12, 2007.
25. Muller HR, Brunholzl C, Radu EW, Buser M. Sex and Side differences of cerebral arteries caliber. *Neuroradiology* 1991; 33:212-216.
26. Caro CG, Doorly DJ, Tarnawski M et al. Non-planar curvature and branching of arteries and non-planars-type flow. *Proc Roy Soc* 1996; 452:185-197.
27. Lee KE, Parker KH, Caro CG et al. The spectral/ hp element modeling of steady flow in non-planar double bends. *Int J Numer Meth Fluids* 2006; 00:1-16.

Figure 1. Geometric criteria defined for the computation of cerebral aneurysm neck orientation with respect to the parent vessel: (A) the normal to the aneurysm bifurcation plane $\mathbf{n}_{an}$ accounts for the neck orientation at the aneurysm site and can be transported along the siphon centerline without introduction of additional torsion by means of parallel transport ($\mathbf{n}_{an\text{-}pt}$); (B) the binormal vectors $\mathbf{b}_{ff}$ of the Frenet frame defined along the siphon centerline identify the local osculating planes; (C) the orientation of the aneurysm neck with respect to the local osculating plane is computed as the angle between $\mathbf{b}_{ff}$ and $\mathbf{n}_{an}$ at the lesion site and the angle between $\mathbf{b}_{ff}$ and $\mathbf{n}_{an\text{-}pt}$ at other locations; (D) locations at which the orientation of the aneurysm neck is evaluated along the siphon centerline: at the aneurysm site and at 2, 4, 6, 8 mm upstream the aneurysm location.

Figure 2A. Curvature (continuous line) and torsion (dashed line) profiles of the ICA centerline of one of the patients included in the study: the points of maximum curvature (square) roughly correspond to locations of low torsion, while the torsion peaks (round) match curvature minima.

Figure 2B. Torsion of curvature maxima and curvature of torsion peaks of all the patients included in the study, relative to the absolute torsion or curvature maxima; curvature maxima exhibit low torsion, while torsion peaks low curvature.

Figure 3. Two views of a 3D model of the ICA, the aneurysm sac and their centerlines; the osculating planes and their normal vectors at points of ICA curvature maxima are also depicted. The carotid siphon can be described as a sequence of near-planar bends separated by sudden changes in the osculating planes orientation.

Figure 4. Length of the individual bends of the carotid siphons once split according to their curvature and torsion profiles. Bends are numbered from the most proximal (bend 6) to the most distal (bend 0, adjacent to the ICA bifurcation). The value at the top of boxes (n) represents the number of patients that exhibit the corresponding number of bends in the tract of ICA being imaged.

Figure 5. Representation of the abscissa of the aneurysm neck ($\mathbf{o}_{an}$) along the ICA centerline for the whole population (all aneurysms) and for ruptured and unruptured groups. The point of zero abscissa is set at each ICA bifurcation, so that centerline abscissas represent distance to the bifurcation. Black dots represent mean value; crosses represent standard deviations.

Figure 6. Distribution of ruptured and unruptured aneurysms on siphon bends. CB represents the *C*-bend that anatomically corresponds to the final bend of the cavernous segment of the ICA; 1p, 2p, 3p and 1d, 2d, 3d represent first, second, third bends respectively proximal and distal to the *C*-bend.

Figure 7. Representation of the distance of the aneurysm neck ($\mathbf{o}_{an}$) from the curvature maximum within the bend hosting the aneurysm for the whole population (all aneurysms) and for ruptured and the unruptured aneurysms. Black dots represent mean value; crosses represent standard deviations.

Figure 8. Representation of the orientation of the aneurysms neck with respect to local ICA geometry by means of the angle computed between the Frenet binormal ($\mathbf{b}_{ff}$) and the aneurysm bifurcation plane normal ($\mathbf{n}_{an}$) at the aneurysm site, and between local Frenet binormals and the aneurysm bifurcation plane normal parallel-transported ($\mathbf{n}_{an\text{-}pt}$) along the ICA centerline at 2, 4, 6, 8 mm upstream the aneurysm site.

Figure 9. Scatterplot (and regression line) of the change in the orientation of the osculating planes defined at the aneurysm site and at 4 mm upstream ($\Delta\alpha_{op}$) against the orientation of aneurysm neck with respect to the ICA geometry at the aneurysm site. Pearson's correlation coefficient and *p*-value are reported.

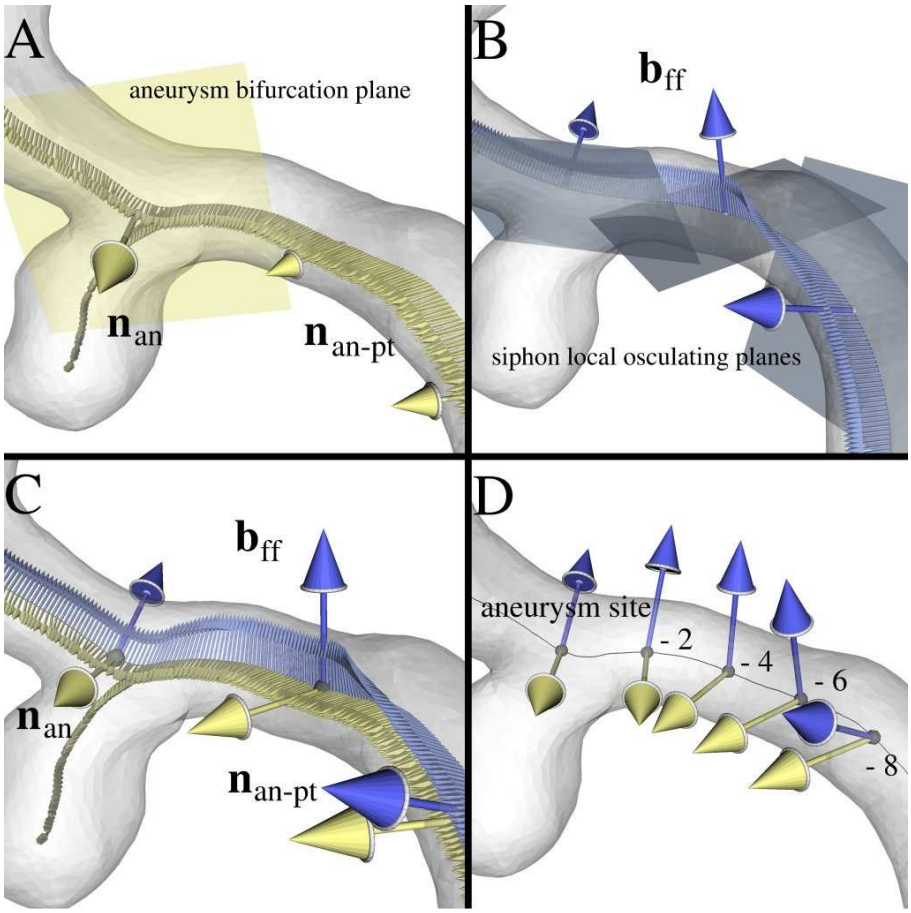
A
aneurysm bifurcation plane
$\mathbf{n}_{an}$
$\mathbf{n}_{an\text{-}pt}$
B
$\mathbf{b}_{ff}$
siphon local osculating planes
C
$\mathbf{b}_{ff}$
$\mathbf{n}_{an}$
$\mathbf{n}_{an\text{-}pt}$
D
aneurysm site
- 2
- 4
- 6
- 8

Figure1.

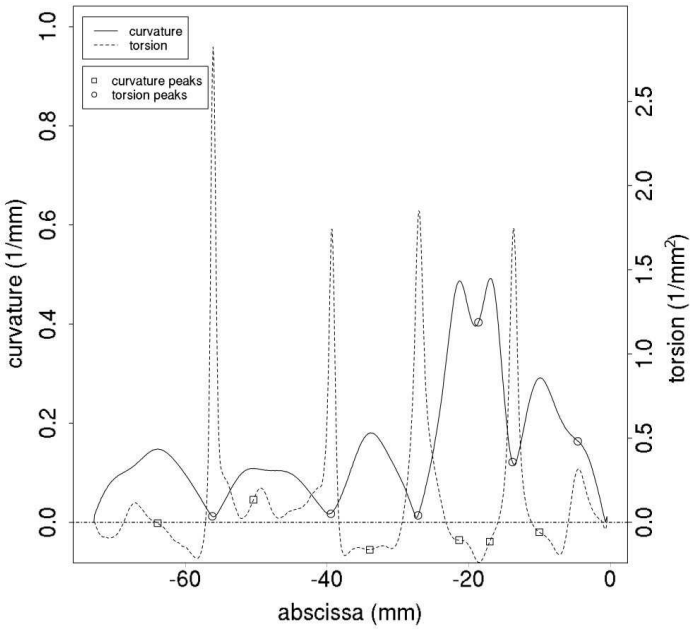

Figure 2A

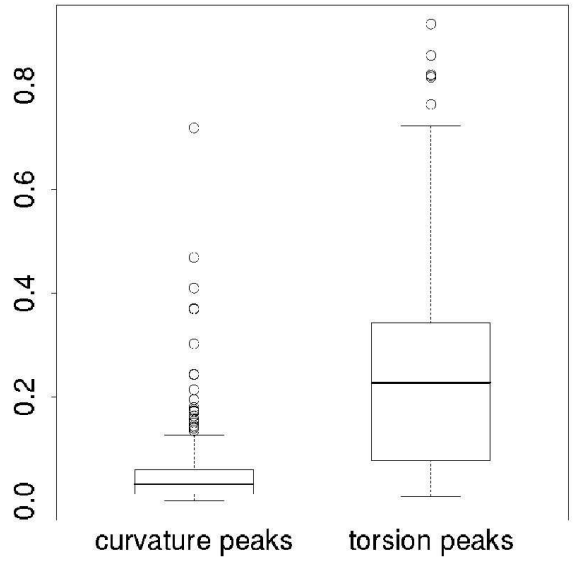

Figure2B

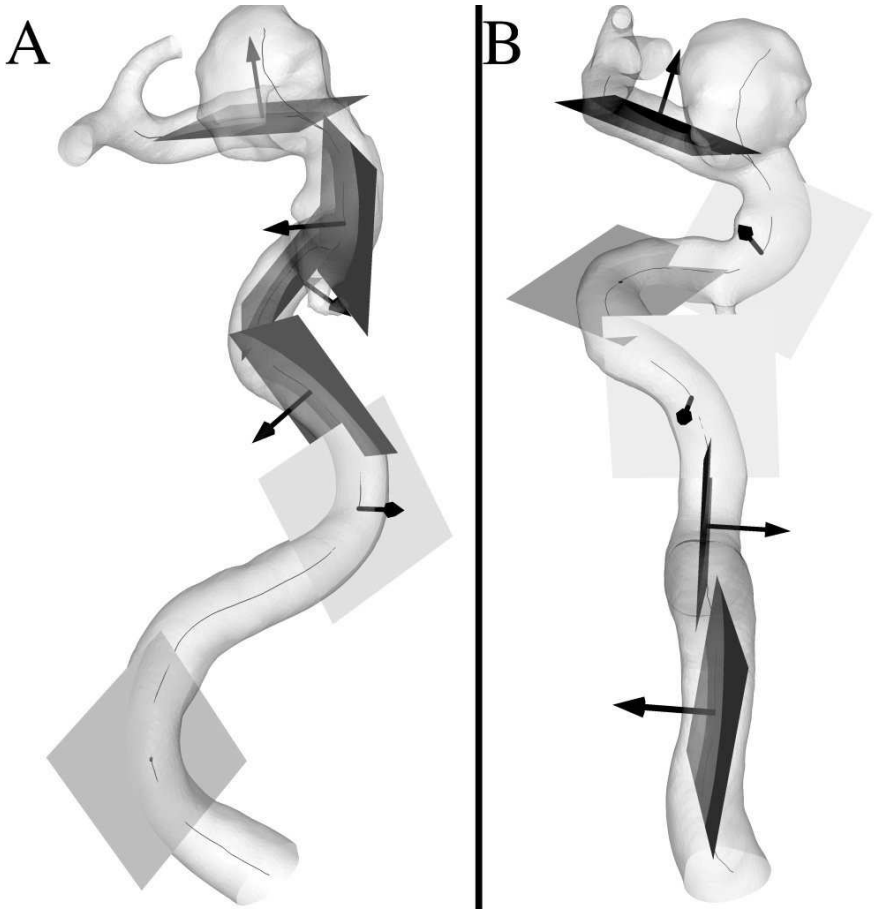

Figure 3.

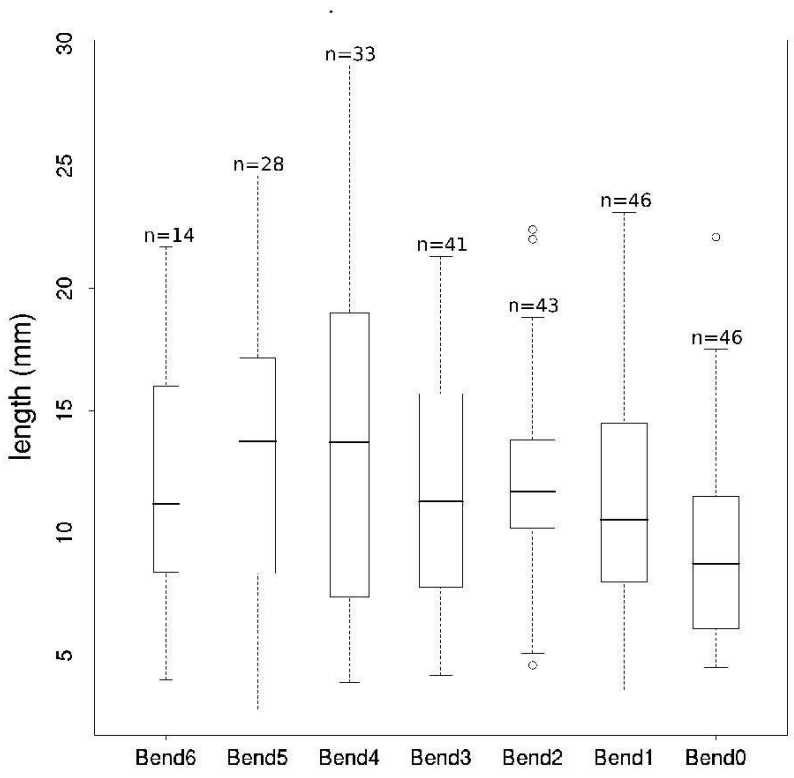
length (mm)
5
10
15
20
25
30
n=14
n=28
n=33
n=41
n=43
n=46
n=46
Bend6
Bend5
Bend4
Bend3
Bend2
Bend1
Bend0

Figure 4.

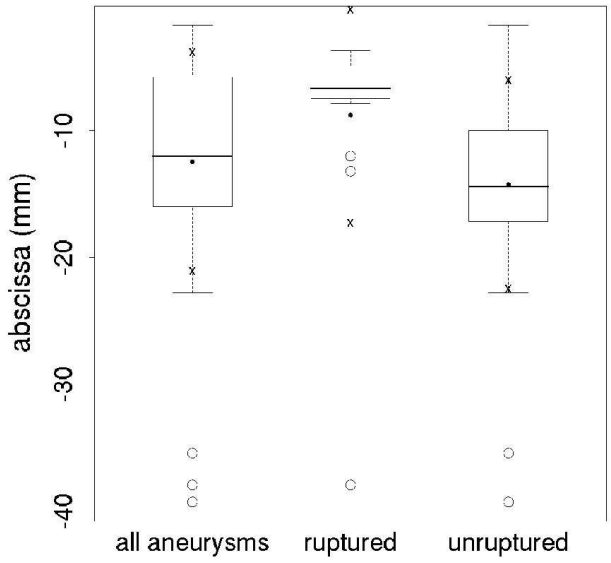

Figure 5.

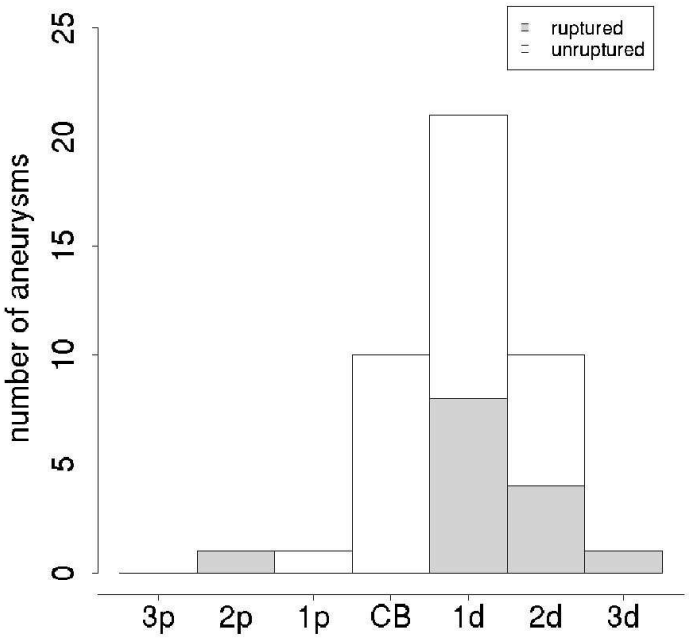

Figure 6.

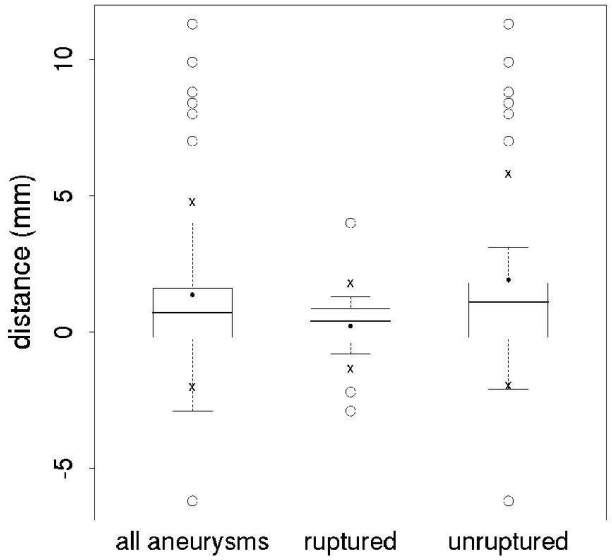

Figure 7.

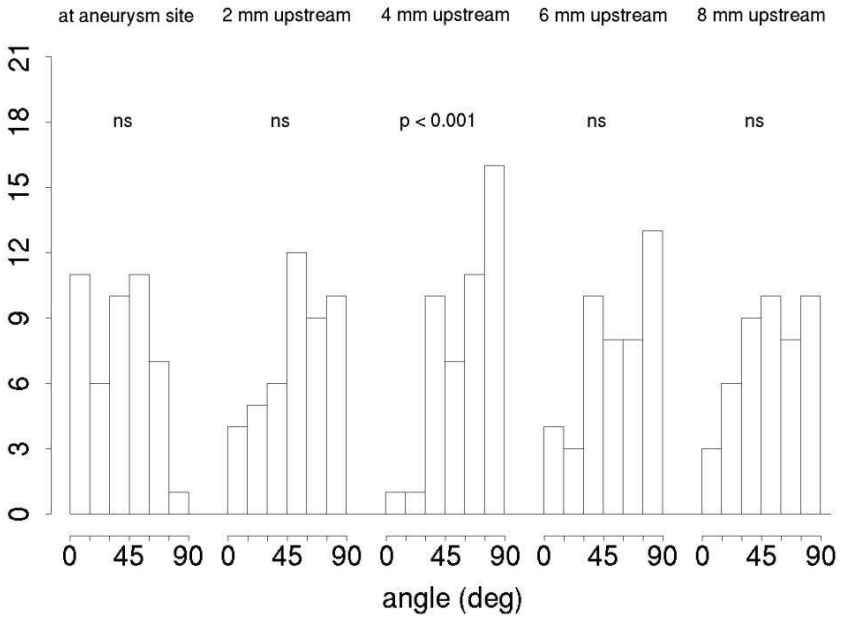

Figure 8.

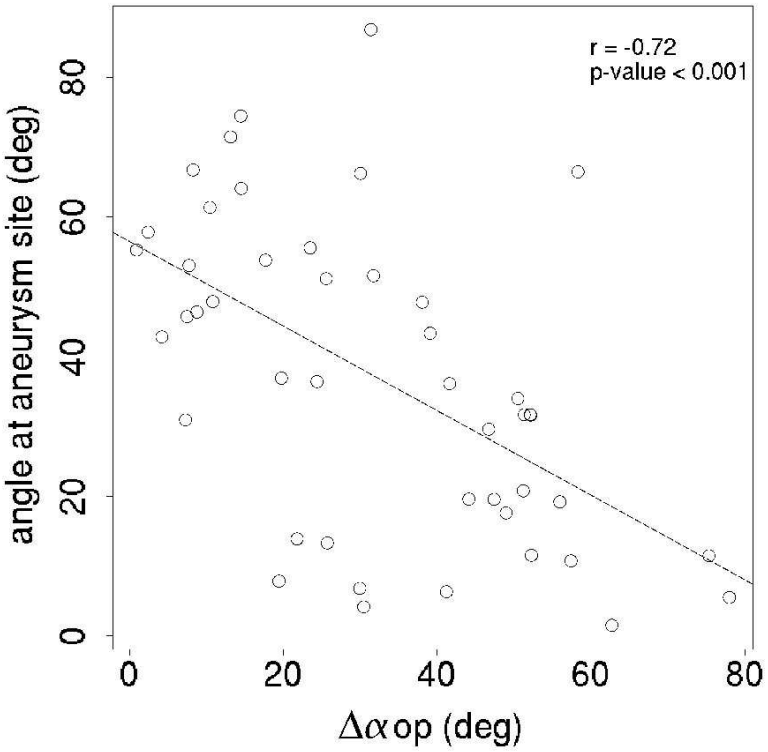
r = -0.72
p-value < 0.001
angle at aneurysm site (deg)
0
20
40
60
80
Δα op (deg)

Figure 9.

Patients demographic data and occurrence of aneurysms

	Subjects	*Aneurysms*	*Age*	*Ruptured*
All patients	134	142	55(14)	67
Female	84	88	55(15)	33
Male	50	54	55(12)	19
Patients with ICA lateral aneurysms	45	46	56(15)	15
Female	37	38	57(16)	12
Male	8	8	52(10)	3

ICA = internal carotid artery

Table 1.